A New Year-Round Weather Regime Classification for North America

SIMON H. LEE,[a] MICHAEL K. TIPPETT,[a] AND LORENZO M. POLVANI[a,b,c]

[a] *Department of Applied Physics and Applied Mathematics, Columbia University, New York, New York*
[b] *Department of Earth and Environmental Sciences, Columbia University, New York, New York*
[c] *Lamont-Doherty Earth Observatory, Columbia University, Palisades, New York*

ABSTRACT: Weather regimes defined through cluster analysis concisely categorize the anomalous regional circulation pattern on any given day. Owing to their persistence and low dimensionality, regimes are increasingly used in subseasonal-to-seasonal prediction and in analysis of climate variability and change. However, a limitation of existing regime classifications for North America is their seasonal dependence, with most existing studies defining regimes for winter only. Here, we normalize the seasonal cycle in daily geopotential height variance and use empirical orthogonal function analysis combined with k-means clustering to define a new set of year-round North American weather regimes: the Pacific Trough, Pacific Ridge, Alaskan Ridge, and Greenland High regimes. We additionally define a "No Regime" state to represent conditions close to climatology. To demonstrate the robustness of the classification, a thorough assessment of the sensitivity of the clustering solution to various methodological choices is provided. The median persistence of all four regimes, obtained without imposing a persistence criterion, is found to be one week, approximately 3 times longer than the median persistence of the No Regime state. Regime-associated temperature and precipitation anomalies are reported, together with the relationship between the regimes and modes of climate variability. We also quantify historical trends in the frequency of the regimes since 1979, finding a decrease in the annual frequency of the Pacific Trough regime and an increase in the summertime frequency of the Greenland High regime. This study serves as a foundation for the future use of these regimes in a variety of weather and climate applications.

SIGNIFICANCE STATEMENT: Weather regimes provide a simple way of classifying daily large-scale regional weather patterns into a few predefined types. Existing methods usually define regimes for a specific season (typically winter), which limits their use, or provides only a minimal assessment of their robustness. In this study, we objectively quantify four weather regimes for use year-round over North America, while we classify near-normal conditions as No Regime. The four regimes represent persistent large-scale weather types that last for about a week and occasionally much longer. Our new classification can be applied to subseasonal-to-seasonal forecasts and climate model output to diagnose recurrent weather types across the North American continent.

KEYWORDS: North America; Climate classification/regimes; Climate variability; Subseasonal variability; Clustering

---

1. Introduction

The fundamental concept of weather regimes, also termed circulation regimes (Straus et al. 2007), is that a small number of recurrent patterns can describe much of the midlatitude atmospheric variability at temporal and spatial scales larger than those of individual weather systems (e.g., Hannachi et al. 2017). At its simplest, the regimes framework classifies the anomalous flow pattern on a given day into *one* of N predefined patterns. Efforts to classify regimes stem back to the mid-twentieth century (Levick 1949, 1950; Lamb 1950; Rex 1951), followed by the diagnosis of regimes using empirical orthogonal functions (EOFs; Vautard 1990; Kimoto and Ghil 1993), and subsequently more complex approaches involving objective clustering methods (Cheng and Wallace 1993; Michelangeli et al. 1995; Cassou et al. 2004) and self-organizing maps (SOMs; Reusch et al. 2007; Bao and Wallace 2015; Francis et al. 2018; Rousi et al. 2021).

At a deeper level, the regimes paradigm aims to capture recurrent, persistent, and quasi-stationary states (Michelangeli et al. 1995; Hannachi et al. 2017). Regimes may represent dynamically stable equilibria (Charney and DeVore 1979; Hochman et al. 2021), although not necessarily (Stephenson et al. 2004; Christiansen 2007; Fereday 2017). Either way, a small number of recurrent anomalous flow states can help "bridge the gap" between the synoptic focus of medium-range prediction and the large-scale climate focus of seasonal prediction. This aspect of "regime thinking" can be contrasted with that of weather "types" (Sheridan 2002; Fereday et al. 2008; Neal et al. 2016), which typically incorporate a larger number of patterns and thus resolve higher-frequency synoptic variability. As a result, regimes-based methods have gained prominence in subseasonal prediction (Grams et al. 2020; White et al. 2021). Owing to their persistence, regimes are well-suited to the weekly time scales typical in subseasonal forecasting, where they can diagnose "windows of opportunity" when extended-range predictability is unusually high (Mariotti et al. 2020).

Despite an increasing number of studies that have analyzed North American weather regimes, they have not been widely adopted, unlike regimes over the North Atlantic–European (NAE) sector. We contend that this primarily arises due to the joint influence of both the Pacific and Atlantic storm

---

Corresponding author: Simon H. Lee, shl2180@columbia.edu

tracks on the North American continent, in contrast to solely the Atlantic storm track influence on Europe. As a result, the foundational work of Michelangeli et al. (1995) defined wintertime regimes in the two basins *separately*. However, doing so yields a complicated description of the flow over North America with two sets of regimes, which undermines the simplicity of the regimes framework.

Following Straus et al. (2007), there is now good agreement among many studies (Vigaud et al. 2018; S. H. Lee et al. 2019; Robertson et al. 2020; Molina et al. 2023) as to the existence of four distinct wintertime regimes centered on North America which capture relevant Pacific *and* Atlantic variability. A notable feature of these classifications is the detection of a regime that resembles the negative North Atlantic Oscillation (NAO), which is otherwise not detected by classifications focusing on upstream Pacific variability (e.g., Fabiano et al. 2021). The inclusion of NAO variability is important given its significant influence on the weather and climate of eastern North America (e.g., Hurrell and Deser 2010).

However, almost all existing analyses of North American weather regimes have focused on the extended winter season, when midlatitude dynamic variability is largest. A few studies have investigated weather regimes in other seasons, but often for targeted, reduced-domain analyses. For example, Zhang and Villarini (2019) defined five year-round weather types over a restricted contiguous United States (CONUS) domain to analyze precipitation extremes in the U.S. Midwest, but did not provide a detailed assessment of the choice of five clusters nor the effect of clustering across multiple seasons. In the context of extended-range prediction of tornado activity over the United States, Miller et al. (2020) used five CONUS-focused regimes for May only. Coe et al. (2021) defined seven weather types over the northeastern United States during autumn and linked these to meteorological impacts and the seasonal transition. More generally, Nabizadeh et al. (2022) defined four summertime regimes over the Pacific–North American (PNA) domain (i.e., excluding Greenland); these showed substantial similarity with the aforementioned wintertime regimes, despite the exclusion of the eastern North Atlantic.

Yet the need to define different regimes for different times of the year (especially during seasonal transition periods) is awkward, and increases uncertainty in the classification given the sensitivity of clustering solutions to methodological choices. To address this issue with the NAE regimes, Grams et al. (2017) developed a set of year-round weather regimes by first removing the seasonal cycle in geopotential height variability prior to EOF analysis and *k*-means clustering. Grams et al. (2017) then applied the regimes to meteorological impacts on European renewable energy generation. Subsequently, the year-round classification has been used to quantify seasonal variation in subseasonal model skill (Büeler et al. 2021), including the contribution of season-specific sources of predictability (such as the stratospheric polar vortex). Other applications outside of winter include identifying circulation types associated with heatwaves in summer (Spensberger et al. 2020) and atmospheric rivers in autumn (Pasquier et al. 2019). It would therefore be advantageous to apply a similar method to the flow over North America, and

rigorously define a new set of year-round regimes for the continent.

This is the goal of the present study. We here define a set of daily, year-round weather regimes in a domain centered on North America. We systematically test the sensitivity of the results to various methodological choices to demonstrate both the robustness of our classification and the reasons for the choices we make. We then link each weather regime to key meteorological variables and other modes of climate variability, and quantify trends and variability in regime frequency since 1979. The regimes defined herein provide a straightforward and reproducible framework, which can be applied across all seasons in operational forecasting and research for a wide variety of purposes.

The rest of the paper is laid out as follows. The datasets, software, and significance testing are outlined in section 2. In section 3, we provide details on the method used to define the regimes. In section 4 we present the new regimes, their characteristics and variability, and relate them to temperature and precipitation anomalies. Our conclusions follow in section 5.

2. Datasets, software, and significance testing

Our analysis is based on the European Centre for Medium-Range Weather Forecasts (ECMWF) ERA5 reanalysis (Hersbach et al. 2020). We use daily mean quantities computed from 6-hourly (0000, 0600, 1200, and 1800 UTC) data (except for daily total precipitation, which is computed using hourly data) over the period 1 January 1979–31 December 2022 on a 1.5° latitude–longitude grid. Daily total precipitation and 2-m temperature anomalies are expressed relative to a 60-day centered running mean climatology. We additionally de-trend 2-m temperature anomalies by subtracting the linear least squares fit to the data for each grid point and calendar day, smoothed with a 60-day running mean. For the large-scale geopotential height fields upon which the regime classification is based, the sensitivity to the choice of modern reanalysis or reasonable variation in grid resolution is likely to be minimal. Time series of the daily NAO index, daily PNA index, and monthly oceanic Niño index (ONI) are obtained from the NOAA Climate Prediction Center website (https://www.cpc.ncep.noaa.gov/products/precip/CWlink/daily_ao_index/teleconnections.shtml). The NAO and PNA indices are renormalized to zero mean and unit standard deviation for the 1979–2022 period under consideration here.

The regimes are computed by *k*-means clustering, using the Python package scikit-learn (Pedregosa et al. 2011) initialized with the *k*-means++ algorithm. The *k*-means method is a widely used and well-established unsupervised learning method for computing atmospheric circulation patterns (e.g., Huth et al. 2008). The algorithm iteratively solves for the set of *k* centroids that minimize the sum of squared Euclidean distances between data points and their corresponding (i.e., nearest) centroids. To minimize the sensitivity of the final clustering solution to the initial seeds, 500 random initializations are used. Convergence of the clustering is declared with a tolerance of 0.0001.

To assess significance of composite statistics associated with the regimes, we account for the persistence of each regime state (i.e., consecutive days with the same regime assignment) by employing block-bootstrapping tests. Each individual "block" of consecutive days assigned to a regime is treated as one object, and then synthetic composites are generated by random resampling of the blocks with replacement 10 000 times. If zero lies outside the 2.5th–97.5th (5th–95th) percentiles of this distribution, then the anomaly is deemed significant at the 95% (90%) confidence level. Elsewhere, simple bootstrapping with replacement is used.

3. Defining the regimes

a. Domain

The choice of a domain for "North America" is a key source of differences among studies of weather regimes over the continent. The domain should be large enough to cover the region of interest, but not too large so as to include atmospheric variability with no direct relevance. We here select the same domain as in the wintertime analysis of S. H. Lee et al. (2019), spanning 180°–30°W, 20°–80°N, which covers almost all of North America from the Aleutian Islands to eastern Greenland, and from central Mexico to the Canadian Arctic. Importantly, this domain includes parts of the eastern North Atlantic so as to include variability associated with the NAO. While analysis of the individual storm tracks may be advantageous from a purely dynamical perspective (as in, e.g., Fabiano et al. 2021), this domain choice is motivated by the relevance to societal impacts and the simplicity of a single regime attribution for the continent. Overall, the regimes presented here are robust to small changes in the domain size (±~20°), following similar testing procedures as in Vigaud et al. (2018) and with a consideration of what might reasonably be defined as "North America."

b. Climatology and anomaly calculation

The regimes are based on 500-hPa geopotential height (Z500) anomalies, which is a common choice for weather regimes. The Z500 anomalies are computed in a three-step procedure. First, we remove the seasonal cycle in the mean state by subtracting a 60-day running mean climatology for each day of the year over 1979–2022. A 10-day low-pass Fourier filter is then applied to the anomalies to emphasize low-frequency variability beyond synoptic time scales. However, the impact of the low-pass filter on the clustering results is relatively small (consistent with Robertson et al. 2020), with 79% of days sharing the same regime attribution if no low-pass filtering is performed.

Next, we detrend the data to account for the increase in the average Z500 owing to thermal expansion of the lower troposphere (Fig. 1a). The data are detrended by removing the linear trend in the daily area-averaged (cosine-latitude weighted) Z500 in the regime domain (5.9 m decade^{-1}; Fig. 1b). We adopt this approach, rather than simply detrending each grid point, in order to retain trends (Fig. 1c) arising from changes in the circulation which may project onto, or alternatively be

caused by, trends in regime frequency. Similar area-averaged detrending methods have been used in previous studies (Fabiano et al. 2021; Dorrington et al. 2022).

Finally, following a similar method to Grams et al. (2017), we normalize by the seasonal cycle in the variance of the Z500 anomalies. The standard deviation of Z500 anomalies across 1979–2022 is computed for each day of the year at each grid point in the regime domain, and then area-averaged with a cosine-latitude weighting. Then, a 60-day centered running mean is applied, and the Z500 anomalies are divided by this scalar as a function of calendar day (Fig. 1d). We perform this normalization to give equal weight to all days within the k-means clustering algorithm; otherwise, the much smaller summertime variance results in these days being weighted less in the clustering solution, because k-means minimizes the sum of within-cluster variances. Relative to other sources of uncertainty, the clustering results are robust to the choice of smoothing window used for the climatology and variance normalization: ~90% of days maintain the same regime attribution for smoothing windows between 0 and 90 days.

c. Principal component analysis

We then perform principal component (PC) analysis on the normalized, low-pass-filtered daily Z500 anomalies, retaining the leading 12 PCs which explain 81% of the total variance. The PCs are not standardized so as to preserve distances. The k-means clustering is then performed in this 12-dimensional PC space, which vastly reduces the dimensionality of the clustering problem and further emphasizes larger-scale variability, while ensuring input variables are uncorrelated. The choice of the number of PCs to retain is arbitrary at this stage; typically, the number of PCs that explain around 70%–80% of the variance are used (e.g., Cassou 2008; Grams et al. 2017), though the clustering solution may not necessarily require all the retained PCs (Lee et al. 2022a; Lembo et al. 2022). Although the variance normalization is performed on the full Z500 anomalies, we also verify that there is no seasonal cycle in the total variance of the 12 PCs used as the basis set for the clustering (not shown).

d. Choosing k

A limitation of the k-means clustering method is the fact that the user must specify the number of clusters, which is not known a priori. The k number can be chosen subjectively by aiming to strike a balance between low dimensionality (for the benefit of predictability), and the representation of finer-scale features that are more tightly linked to local surface weather modulation. However, several objective, data-driven methods exist for determining the best number of clusters, and hence the number of regimes. Here, we offer four different methods which all support the same choice of $k = 4$.

The simplest is to run the clustering algorithm to convergence for a range of k, and find the largest k for which the Pearson correlation between the centroid coordinates in PC space is less than zero (i.e., the largest number of clusters for which the patterns are all anticorrelated). This threshold maximizes the number of clusters while limiting feature repetition

(a) Full trend

(b) Domain-average Z500 & trend

(c) Residual trend

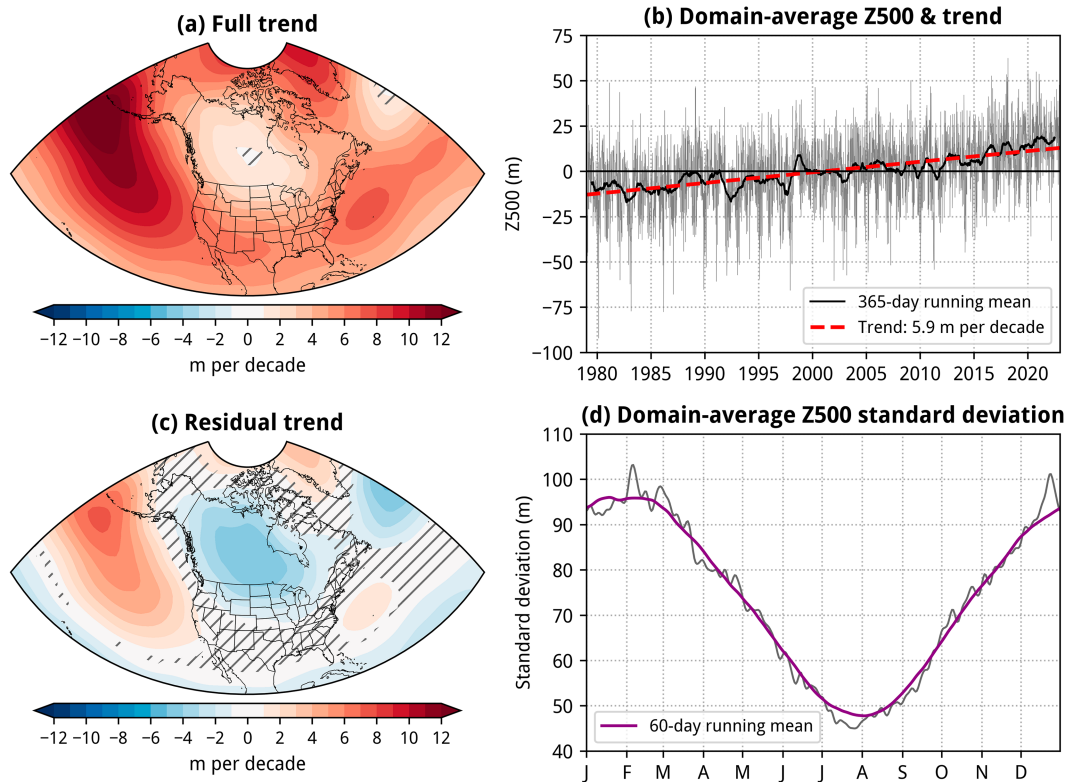**(d) Domain-average Z500 standard deviation**

FIG. 1. (a) Linear trend in daily Z500 anomalies at each grid point in the regime domain from 1 Jan 1979 to 31 Dec 2022. (b) Daily area-averaged Z500 anomalies in the regime domain (gray), a 365-day centered running mean (black), and the linear trend (5.9 m decade^{-1}; red, dashed). (c) Residual trends in daily Z500 anomalies when the trend in (b) is subtracted. (d) Area-averaged standard deviation of Z500 anomalies as a function of calendar day (gray), with a 60-day centered running mean (purple). Hatching in (a) and (c) denotes trends that are not significantly different from zero at the 95% confidence level according to 10 000 bootstrap resamples with replacement.

between clusters (motivated by seeking the smallest number of clusters required to capture the dominant flow patterns). Figure 2a shows that this method yields $k = 4$.

A second approach is the measure proposed by Davies and Bouldin (1979), defined for k clusters following:

$$\mathrm{DB}(k) = \frac{1}{k} \sum_{i=1}^{k} \max_{i \neq j} \left(\frac{s_i + s_j}{d_{ij}} \right), \tag{1}$$

where s_i is the average distance between members of cluster i and the centroid of that cluster, and d_{ij} is the distance between the centroids of cluster i and j. The DB index therefore represents the average similarity between one cluster and its most similar cluster. Hence, the optimal choice of k is one which minimizes the index, indicating the clusters are well separated. Figure 2b shows that this method also clearly yields $k = 4$ as the best choice.

The third approach presented here (Fig. 2c) is the "classifiability index" introduced by Michelangeli et al. (1995, hereafter MVL95). The classifiability index tests both the robustness of the clustering solution to the initial seeds *and* the extent to which the solution can be distinguished from synthetic noise data. We follow a slightly modified version of the

method of MVL95, which we detail here in full. For the 12 PCs, for a given value of k, the k-means algorithm is initialized 1000 times from 1000 different random seeds, to produce 1000 different partitions of the data. (The choice of 1000—20 times that of MVL95—is arbitrary, but was chosen to obtain more stable classifiability statistics given the much longer dataset here.) Clusters are matched to each other between all combinations of partitions by finding the maximum correlation between the centroids. Then, the minimum correlation between a cluster in one partition and its equivalent in another partition is stored each time. These minima are averaged to yield the classifiability $c^*(k)$. Similar to MVL95, we also compare the results with a reference noise model, computed as 12 first-order autoregressive [AR(1)] processes with the same variance and lag-1 autocorrelation as each of the 12 PCs. One hundred such synthetic time series are created and $c^*(k)$ is computed for each. The best choice of k for the atmospheric data is therefore the smallest k that has both high classifiability (i.e., low dependence on the initial seeds) and higher classifiability than the noise data. Only $k = 3$ ($c^* = 0.98$) and $k = 4$ ($c^* = 0.97$) show high classifiability. However, $k = 4$ is much more classifiable than the equivalent AR(1) data, with c^* greater than 93% of the AR(1) time series (consistent with the one-sided 90% test used by MVL95)
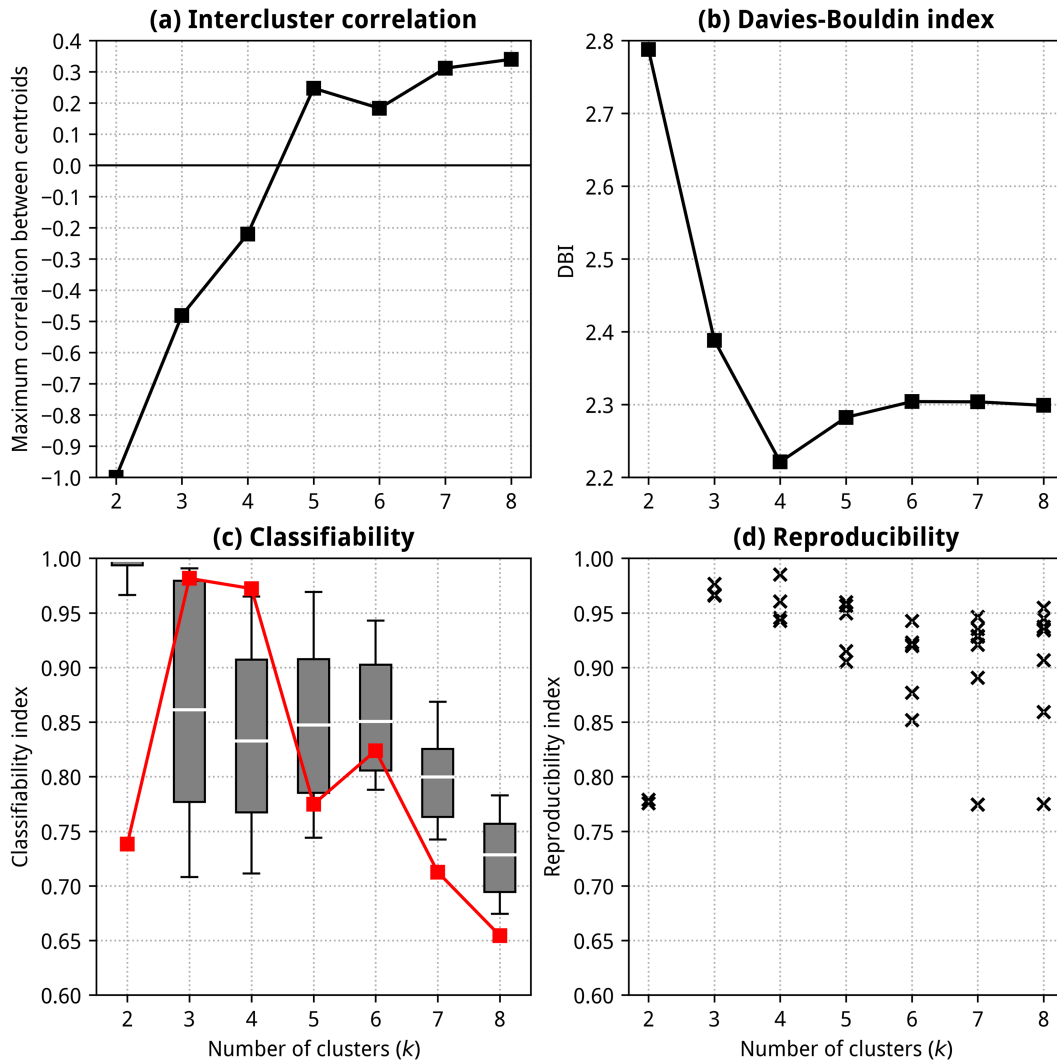
FIG. 2. For k ranging from 2 to 8: (a) the maximum correlation between cluster centroids; (b) the Davies–Bouldin index (see main text for details); (c) the classifiability index $c^*(k)$ computed using the 12 PCs (red line) and boxplots of $c^*(k)$ obtained from 100 sets of 12 AR(1) time series modeled on the PCs, with whiskers extending between the 10th and 90th percentiles; and (d) the reproducibility index for each cluster obtained from 1000 random draws of 22 years from the full dataset.

versus only 77% for $k = 3$. Hence, the classifiability test also indicates $k = 4$ is the best choice.

Finally, again following MVL95, we compute a "reproducibility index." This index quantifies the extent to which the centroids are dependent on the specific choice of input data length, by assessing whether a similar clustering solution can be obtained from a smaller subsample. Half the data (22 years, not necessarily consecutive) are randomly sampled without replacement, and k-means clustering is computed for k ranging from 2 to 8. The centroids from each subsample are matched to those computed from the full dataset by finding the maximum correlation between the two partitions. This is then averaged for each cluster across 1000 random samples to yield the reproducibility index for each centroid of a given k-cluster set (Fig. 2d). As noted by MVL95, the reproducibility and classifiability indices give similar results, and here

we find $k = 4$ is the largest k for which all clusters are highly reproducible.

From this analysis, we conclude that $k = 4$ is the most appropriate number of regimes for use year-round in the North American sector. Choosing a larger k results in clusters that are less classifiable, less reproducible, and less distinct from one another. We note that $k = 4$ has also been previously shown as optimal for use in winter [e.g., the classifiability index analysis in Vigaud et al. (2018)], which implies the same number of preferred flow patterns over North America regardless of season. Indeed, if the four wintertime regimes are robust and not a statistical artifact, then it could be argued that the number of year-round regimes should include these and thus be *at least* four. However, in contrast to the seven year-round NAE regimes of Grams et al. (2017), none of the
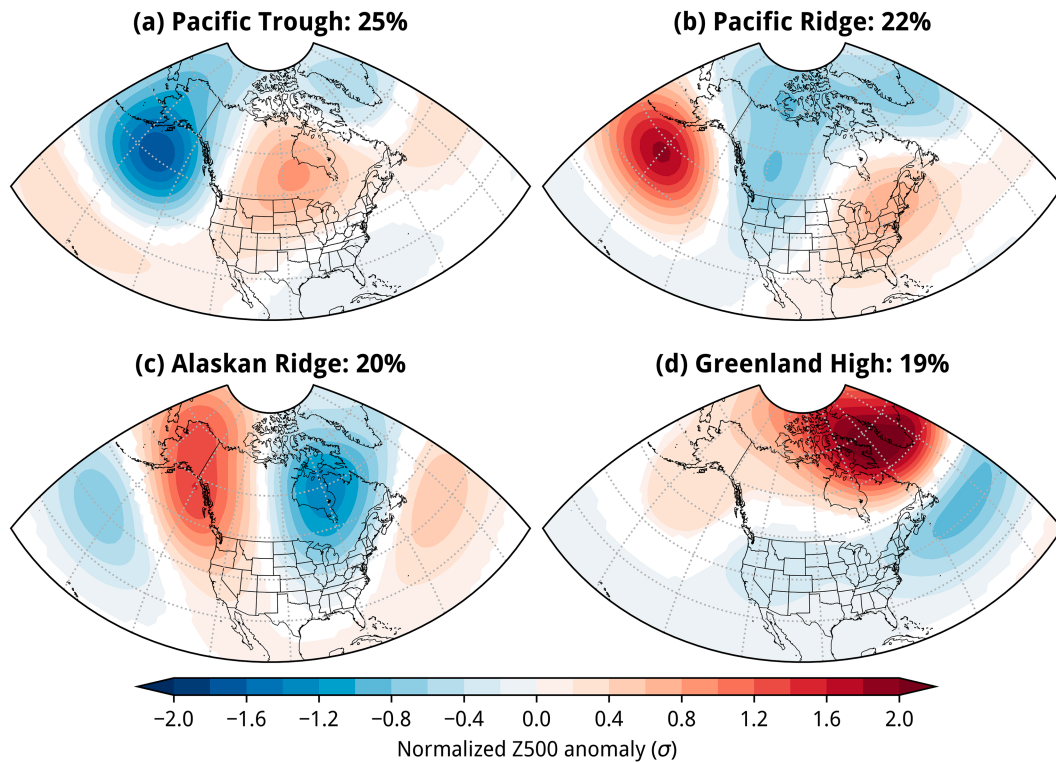
FIG. 3. Average normalized Z500 anomalies for all days assigned to the (a) Pacific Trough (PT), (b) Pacific Ridge (PR), (c) Alaskan Ridge (AKR), and (d) Greenland High (GH) regimes. Percentages denote the overall frequency of each regime during 1979–2022 (total 86%; remaining 14% classified as "No Regime"). Data are masked where not significantly different from zero at the 95% confidence level according to a block bootstrap resampling test.

four objective methods presented in Fig. 2 suggest more than four year-round North American regimes can be reliably obtained using k-means clustering.

4. The four year-round North American regimes

a. Regime assignment

Using $k = 4$, each day is assigned to a cluster by the minimum Euclidean distance to a cluster centroid. Naive clustering assigns *every* day to a cluster, and thus *every* day into a regime—including days where the anomalies are negligible and do not closely resemble a cluster mean. Therefore, we define a fifth cluster centroid with all PCs set to zero to represent the climatological state. Then, any days which are closer to this new centroid than any of the other four centroids (by Euclidean distance) are classified as "No Regime." This is an objective and straightforward classification of a neutral state which operates in the same space as the naive cluster assignment and does not depend on an arbitrary threshold. Furthermore, rerunning the clustering without the No Regime days yields the same four patterns and the same regime assignment on 99.6% of days, confirming that the subsequent reclassification would not otherwise influence the k-means solution.

b. Regime patterns

The cluster-mean normalized Z500 anomalies for the four regimes are shown in Fig. 3; the mean anomalies during No Regime are negligible, and thus not shown. (Nonnormalized, seasonally varying Z500 anomalies are discussed later in section 4g, but can be recovered for any day of the year here by multiplying by the relevant scalar from Fig. 1d.) These four regimes are very similar to the set of four previously identified for the winter. Such similarity is perhaps surprising, but the summertime North American regimes identified by Nabizadeh et al. (2022) do not differ greatly from their winter counterparts. Moreover, a set of year-round regimes should at least include the wintertime regimes, and so if there are both four wintertime regimes *and* four year-round regimes, then the patterns should be extremely similar. We also found that four almost identical regimes can be obtained by using a 4×1 SOM of the normalized Z500 anomalies without an EOF transform (not shown), providing further evidence of the robustness of the classification.

In the existing literature, the same regime patterns have been given different names [compare, for example, Robertson et al. (2020) with Straus et al. (2007)]. Here, we adopt a naming convention based on a combination of the location of the largest-magnitude anomaly and some element of continuity with names used in previous studies. We refrain from naming any of the regimes by their similarity to modes of variability (such as the PNA or NAO) to avoid potential confusion with index time series. From most-to-least frequent overall, the regimes are named the Pacific Trough (PT, occurring on 25% of
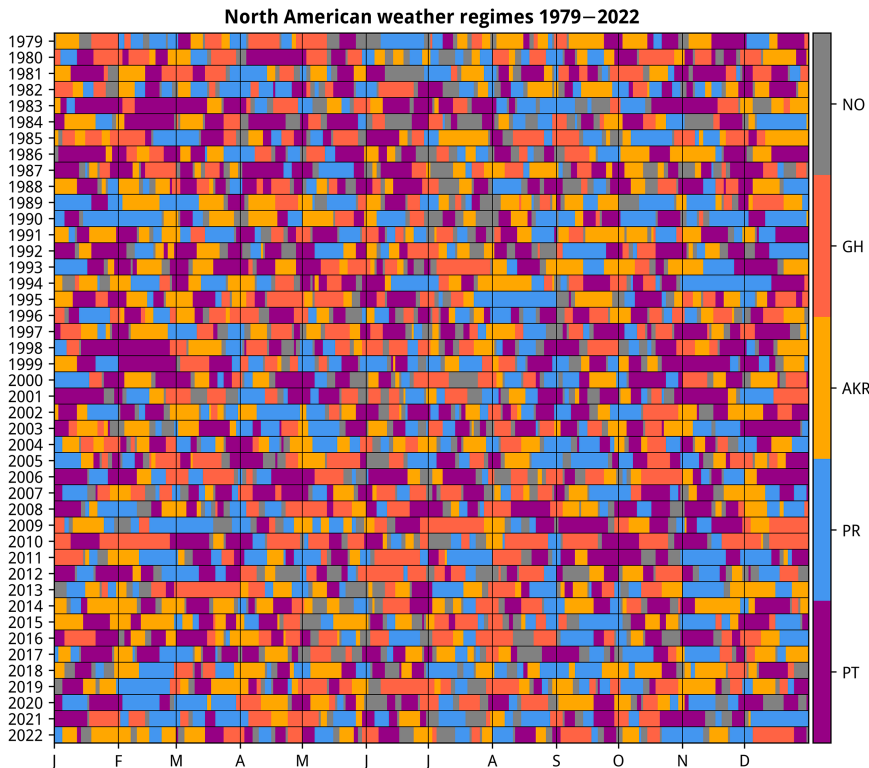
FIG. 4. Daily year-round North American weather regime attribution from 1 Jan 1979 to 31 Dec 2022.

days), the Pacific Ridge (PR, 22%), the Alaskan Ridge (AKR, 20%), and the Greenland High (GH, 19%). No Regime accounts for the remaining 14% of days. A graphical depiction of the daily regime classification over 1979–2022 is shown in Fig. 4.

As these regimes patterns are broadly similar to season-specific patterns described elsewhere, we only briefly summarize their key characteristics here. The PT regime (Fig. 3a) consists of an anomalous trough in the Gulf of Alaska, associated with an enhanced meridional Z500 gradient in the northeast Pacific. An anomalous ridge, centered over Manitoba, dominates the flow over the bulk of the United States and Canada, while a modest cyclonic anomaly can be found over central Greenland and the southeastern United States. The PR regime (Fig. 3b) is characterized by almost equal-and-opposite anomalies to the PT regime in the northeast Pacific, with an anomalous ridge south of the Aleutian Islands. However, across the continent, the configuration is rather different: the high latitudes from Alaska to Greenland are dominated by a cyclonic anomaly which extends down the western half of the continent, with an anomalous ridge downstream centered on New York state. The AKR regime (Fig. 3c) consists of a wave train extending from the Pacific to the Atlantic, with the continent dominated by a dipole between the anomalous ridge over Alaska and trough over the Hudson Bay, yielding an anomalously meridional flow. The ridge–trough pattern of the AKR regime constructively interferes with the mean stationary wave present over North America, generally opposite to the broadly destructive interference by the PR

regime. Finally, the GH regime (Fig. 3d) consists of a large negative NAO-like anticyclonic anomaly centered over the Labrador Sea extending west with diminishing amplitude to Alaska. Most of the United States lies under anomalously low Z500, with the cyclonic anomalies maximizing to the southeast of Atlantic Canada. The GH regime differs from the other regimes by showing only minimal anomalies in the northeast Pacific.

c. How many PCs?

As mentioned in section 3c, the choice of 12 PCs as the dimension of the clustering space was somewhat arbitrary, so we now seek to quantify how many PCs are in fact necessary to recover an equivalent cluster solution for $k = 4$. Figure 5a shows the coordinates of the cluster centroids in the leading 12 PCs of the normalized Z500 anomalies (cf. Lee et al. 2022a, their Fig. 2e, for an equivalent analysis of the winter-time regimes). The coordinates are close to zero for all but the leading three PCs, and thus only the leading three PCs contribute significantly to defining the regime centroids. To quantify the impact of each additional retained PC to the clustering solution, we recompute the four clusters using 1–12 PCs, and compute the area-weighted pattern correlation between the cluster-mean Z500 anomalies for each regime and the corresponding 12-PC composites. Figure 5b shows that, for clustering solutions performed with at least the leading three PCs, the pattern correlations all exceed 0.99. The third PC is primarily required to obtain the PR and AKR regimes, while the GH and PT cluster-mean anomalies are largely obtained with
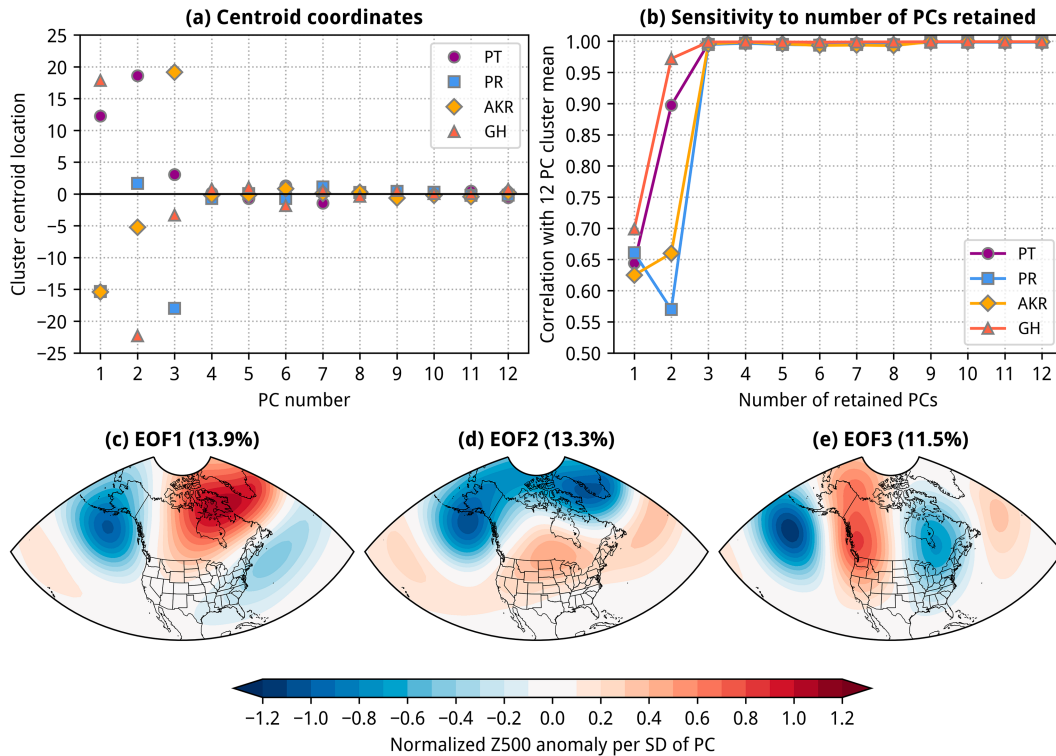
FIG. 5. (a) Coordinates of the $k = 4$ regime centroids in 12-dimensional PC space. (b) Sensitivity of the cluster solution (with $k = 4$) to the number of retained PCs from 1 to 12, expressed as the area-weighted pattern correlation of the cluster-mean Z500 anomalies with the cluster means obtained from 12 PCs. (c)–(e) Regression of the standardized PC time series for EOFs 1–3 with the variance-normalized Z500 field, and the percent of the total variance explained by each EOF.

only two PCs. The minimal contribution of the third PC to the GH and PT regimes can be verified by noting the comparably small magnitude of their centroids in PC3 (Fig. 5a). As a result, a time series of the regimes computed by clustering only the leading three PCs yields the same regime on 95% of days as that based on 12 PCs.

Therefore, the regimes defined herein are effectively governed by only the leading three EOFs, which together explain 39% of the variance in the daily low-pass-filtered normalized Z500 anomalies. Maps of the EOFs are shown in Figs. 5c–e: these bear some similarities with established patterns of variability such as the PNA and NAO, but we caution the EOF transform here is not performed with a view to represent such physical modes. We also emphasize that, unlike EOFs, the regimes do not have a positive and negative loading, and are not orthogonal or uncorrelated. Nevertheless, at their simplest, the regimes can be interpreted as a linear combination of these EOFs.

d. Persistence and transitions

A key aspect of the regime framework is the persistence of a single regime for time scales greater than individual, synoptic-scale weather systems (Vautard 1990). The regimes identified here are not obtained using an a priori minimum persistence criterion: the only explicit temporal filtering is the 10-day

low-pass filter of the Z500 anomalies prior to clustering (although the truncated PC basis acts as an implicit temporal filter). Hence, the persistence of each regime reflects an intrinsic property of the large-scale flow, and is not an arbitrary choice in the construction.

The distribution of durations of all regime instances, defined as the number of consecutive days with the same regime assignment, is shown in Fig. 6a alongside an equivalent analysis for No Regime. The median duration of all four regimes is around one week (7 days for PT and GH, and 6 days for PR and AKR), and the middle 50% of all regime instances persist for 4–10 consecutive days. In contrast, the median duration of No Regime is only 2 days, and 75% of such instances persist for less than 5 consecutive days. Therefore, the regime classification identifies more persistent states with a typical weekly time scale. Extremely long-lived regimes—lasting for more than 3 weeks—also occur, with an overall maximum of 44 consecutive days of the PR regime ending 14 December 1994. We note that, if no low-pass filter is applied, the median duration of the four regimes decreases to 4 days, primarily due to a greater frequency of regimes lasting for less than 5 days. Hence, the 10-day filter is effective in its purpose at suppressing the influence of synoptic-scale variability.

Next, for each regime R at lag d from regime onset, Fig. 6b shows the probability of being in regime R on day d conditional
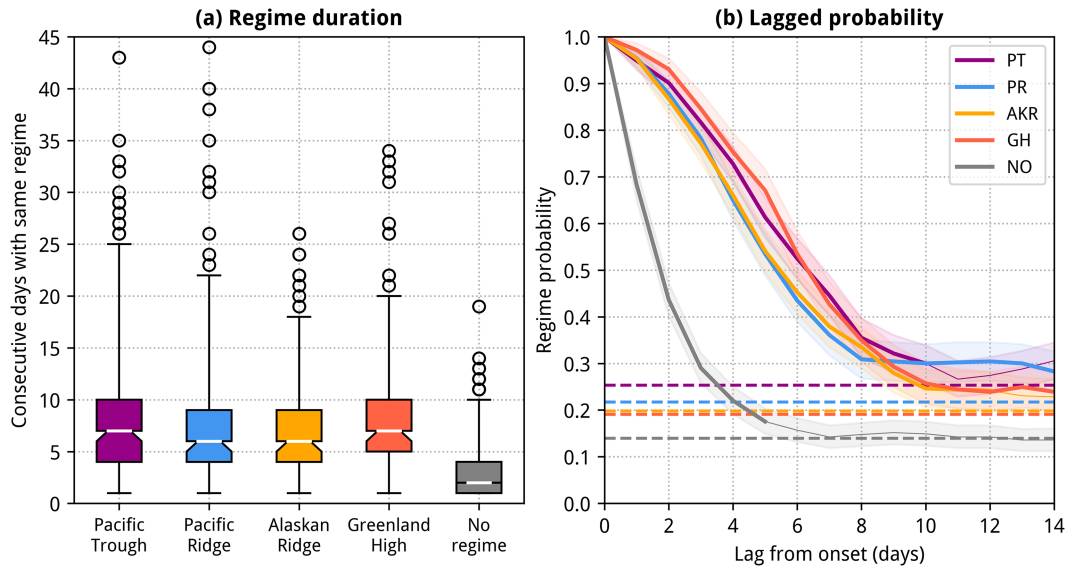
FIG. 6. (a) Boxplots of regime duration, defined as consecutive number of days with the same regime assignment. White horizontal lines denote the medians and notches denote 95% confidence intervals obtained by bootstrapping. Whiskers extend between the 2.5th and 97.5th percentiles, with open circles denoting outlier points. (b) Probability of each regime as a function of lag from the first day assigned to each regime. Dashed horizontal lines denote the climatological probability of each regime. Shading denotes 95% confidence intervals obtained by bootstrapping; lines are thickened where the climatological frequency lies outside this interval.

on being in regime R at $d = 0$, regardless of the regime attribution in between. In contrast with Fig. 6a, this analysis does not require *consecutive* days of the same regime and incorporates cases where regimes decay and subsequently recur. All four regimes are significantly more likely than climatology for at least 10 days after the onset of a regime; the probability of the PR and GH regimes remains elevated above climatology for 14 days (and decays thereafter). In contrast, the probability of No Regime rapidly decays to climatology by 5 days (well approximated by an exponential function with an *e*-folding time scale of 2.5 days).

We next quantify the frequency of regime transitions (a 5×5 matrix), shown in Fig. 7. We urge caution in interpreting these results because the persistence of the regimes results in very small sample sizes (widely <100) for each individual transition, and the seasonality of the regime frequencies likely leads to seasonality in the transition probabilities which are not captured here. Nevertheless, it is notable that transitioning into No Regime is clearly the most likely transition for all four regimes. Hence, because of the definition of No Regime used here, this means that regimes tend to terminate by decaying toward climatology, rather than transitioning directly via a "mixed" state (in which different aspects of two regimes are simultaneously amplified). This behavior is consistent with our regime classification identifying large-scale quasi-stationary states, rather than propagating synoptic-scale weather systems. A lack of transition symmetry is also evident: for example, the transition from GH to AKR (3.3%) is more than twice as likely as the reverse (1.4%; the least likely of all transitions, having only occurred 45 times in 44 years). The relatively higher likelihood of the GH to AKR transition is consistent with

the westward propagation of a high-latitude anticyclone under the weak zonal flow typical of the GH regime. Similarly, the preference for transitions between the AKR regime and either the PT or PR regimes is dynamically consistent with the propagation of a Rossby wave train.

e. Relationship with the NAO, PNA, and ENSO

Having presented the new regimes and their persistence, we now relate them to the widely known and well-established NAO and PNA teleconnection indices by computing the frequency of each regime conditional on the contemporaneous sign of the NAO and PNA indices. We use a simple $\pm 0.5\sigma$ threshold to define the positive and negative phases of those indices.

The GH regime exhibits the strongest relationship with the NAO (Fig. 8a), with a probability of 51% given a negative NAO index. All other regimes are much less likely during a negative NAO than during either a neutral or positive NAO. The PT, PR and AKR regimes are all equally likely during a positive NAO (30%), while the GH regime is effectively absent (<1%). For the PNA (Fig. 8b), the PT and PR regimes show almost equal-and-opposite behavior, with the PT most likely given a positive PNA (43%) and the PR most likely given a negative PNA (44%). There is only a weak relationship between the PNA and the AKR regime (16% for a negative PNA and 21% for positive PNA), and there is no relationship between the PNA and the GH regime. As might be expected, No Regime is most frequent when the teleconnection indices are near neutral. Hence, aside from the strong relationship between the GH regime and the negative NAO, this analysis demonstrates the diversity of weather patterns

FIG. 7. Matrix showing the frequency of transitions (%) from each regime (rows) to other regimes (columns). The self-transition frequencies (i.e., lag-1 persistence frequencies) are shown in bold white font on the main diagonal, while the most likely transition for each regime is shown in bold black font.

that can exist for a given PNA or NAO index. Indeed, as noted by Grams et al. (2017) for the NAO, it could be misleading to expect a particular weather pattern based solely on a given PNA or NAO index (either alone or in combination), or to equate indices and regimes: they are not equivalent, as this analysis demonstrates.

Given the large role of ENSO in modulating North American climate and prior work linking ENSO to extratropical weather regimes (e.g., Molteni et al. 1993; Straus et al. 2007), we next show in Fig. 8c the probability of each regime given the concurrent ENSO state. Since we are considering year-round data but ENSO variability exhibits a pronounced seasonality, we classify El Niño and La Niña by the outer quartiles of the ONI distribution for each overlapping 3-month period (similar to Tippett and Barnston 2008). The PR regime displays the strongest ENSO dependence; it is around 50% more likely during La Niña versus El Niño, consistent with its similarity with the negative PNA pattern, and is the least likely of the four regimes during El Niño. The PT regime demonstrates a weaker reverse relationship, being 20% more likely during El Niño versus La Niña. There is also a weak suppression of the AKR regime during La Niña (during which it is the least frequent regime), but no ENSO-dependent modulation of the GH regime nor the No Regime state. While we do not perform them here, similar analyses could also be performed for other key modes of climatic variability and predictability, such as the Madden–Julian oscillation (e.g., Cassou 2008; R. W. Lee et al. 2019).

f. Seasonal variability

The construction of the regimes as year-round phenomena does not preclude seasonal variability in their relative frequencies,
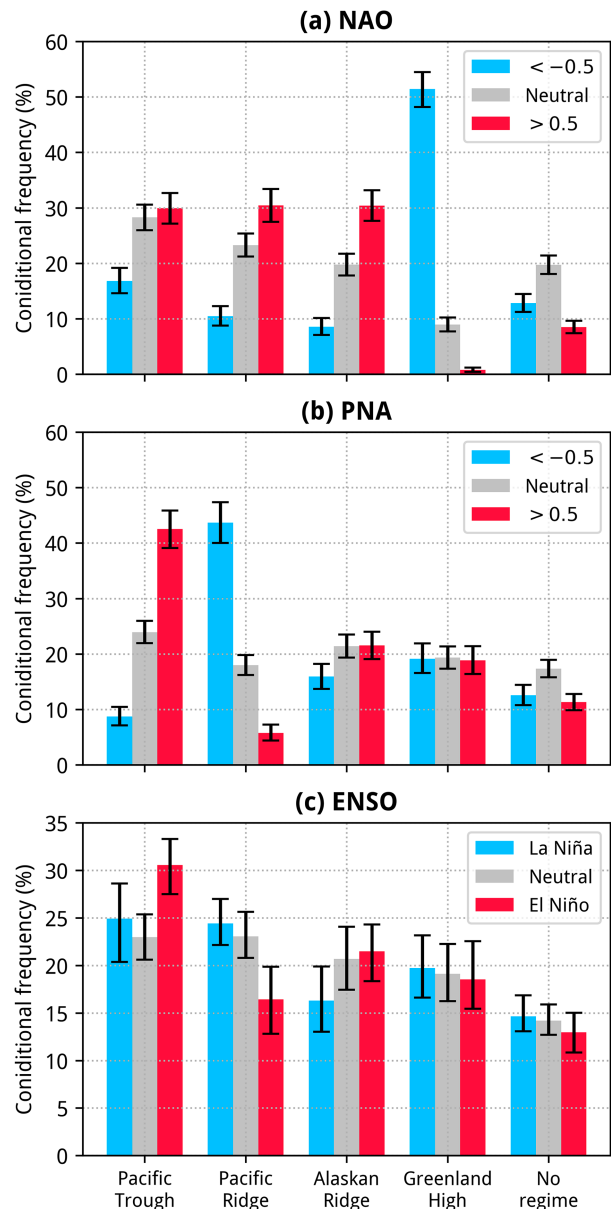

FIG. 8. Probability of each regime subset by the state of the (a) NAO, (b) PNA, and (c) ENSO. In (a) and (b), a simple $\pm 0.5\sigma$ threshold is used; in (c) the seasonally varying 25th and 75th ONI percentiles are, respectively, used to define La Niña and El Niño. Error bars indicate 95% confidence intervals obtained by block bootstrapping. Note the different *y* axis in (c).

as shown in Fig. 9 for overlapping 3-month periods. The PT regime is more frequent in the cold season, with a maximum frequency in OND (30%) and a minimum in JJA (19%). The AKR regime displays a similar seasonality, with a peak frequency in NDJ and DJF (24%) and a minimum in MAM (16%). The GH regime is most frequent in the late spring and early summer (peak frequency in MAM of 24%) and least frequent during the cold season (15% in OND). Unlike the other three regimes, there is no notable seasonality to the frequency
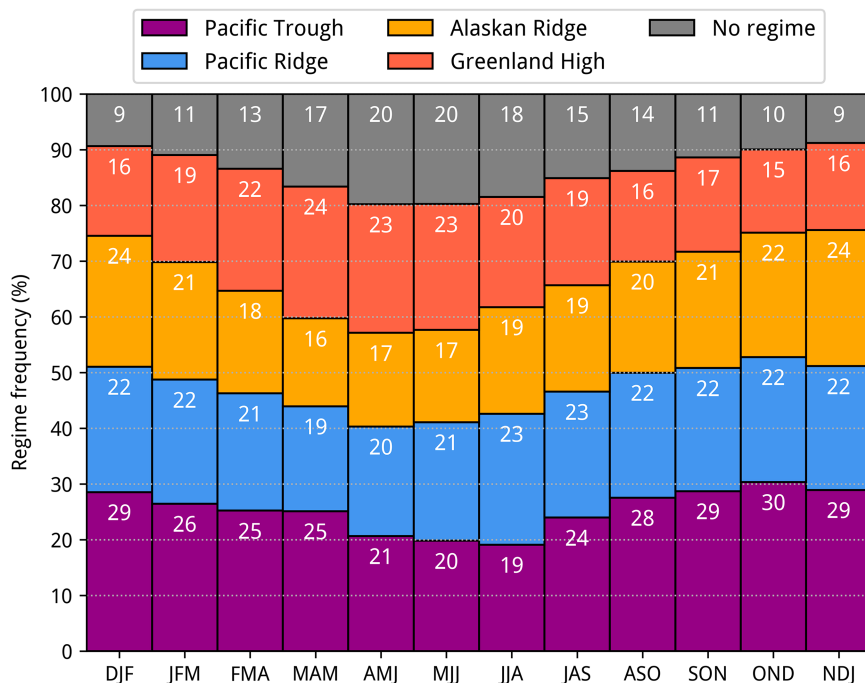
FIG. 9. Seasonal variation in the frequency of the weather regimes, calculated over centered 3-month periods. Numbers in each bar segment denote the percent of days in each 3-month period assigned to each regime.

of the PR regime (overall range of only 4 percentage points). We also assessed seasonal variability in persistence, but found the differences to be generally small: for all regimes, the median duration varies between seasons by no more than ± 1 day relative to the overall median. However, long-lasting PT and PR regimes are more likely during winter, when the top 25% longest regimes last for more than 2 weeks, versus 8–10 days in other seasons.

The springtime peak in GH frequency is consistent with the downward influence of final stratospheric warmings (Black et al. 2006; Butler and Domeisen 2021), given the increased likelihood of the similar wintertime regime during weak stratospheric polar vortex conditions (S. H. Lee et al. 2019). Seasonality in the magnitude of ENSO forcing may explain the lower frequency of the PT regime in summer (given its link to El Niño, Fig. 8c), but an equally simple argument cannot be applied to the PR regime (given its link to La Niña) since it displays no seasonality. The maximum in the frequency of No Regime during early summer (20%; twice as frequent as during winter), suggests that the summertime flow is fundamentally less regime-like, which may be expected from the weaker large-scale variability structures in summer (Wallace et al. 1993). Importantly, the summertime No Regime peak occurs despite the variance normalization of the Z500 anomalies, which means that it is not the result of reduced variance. Otherwise, in the absence of variance normalization, No Regime would account for almost 50% of summer days and thus simply reflect the seasonality in Z500 anomaly magnitude, rather than being a meaningful classification of summertime variability. We also note that a proportionate increase in the frequency of No Regime (albeit defined differently) occurs during summer in the year-round NAE regimes of Grams et al. (2017), while Büeler et al. (2021) found that No Regime states in the NAE region were associated with reduced forecast skill. Hence, the summertime peak in the frequency of No Regime may contribute to the generally lower summertime extratropical large-scale prediction skill (Son et al. 2020; Büeler et al. 2021).

Despite the seasonality in their frequency, the spatial patterns of the regimes do not markedly change (aside from the seasonal cycle in the magnitude of the Z500 anomalies). For each season and regime, Fig. 10 shows the nonnormalized cluster mean and its median area-weighted pattern correlation with the Z500 anomalies of the days assigned to that regime. The year-round classification performs well in all seasons: the seasonal-mean patterns do not differ substantially from the year-round means (cf. Fig. 3; all pattern correlations > 0.93) and the median correlations with the respective seasonal means vary by no more than 0.13. We also note the good degree of correspondence between the JJA patterns here and the four extended summer (JJAS) regimes defined by Nabizadeh et al. (2022), despite their more Pacific-centric domain.

To objectively verify that our year-round approach captures the same patterns that would appear by constructing regimes for each season separately, we also computed $k = 4$ seasonally dependent regimes (plus no regime, defined as for the year-round set) using the leading 12 PCs of nonnormalized, low-pass-filtered Z500 anomalies for each season. We then compared these with the maps in Fig. 10, and confirmed that the same four patterns are detected in each season: area-
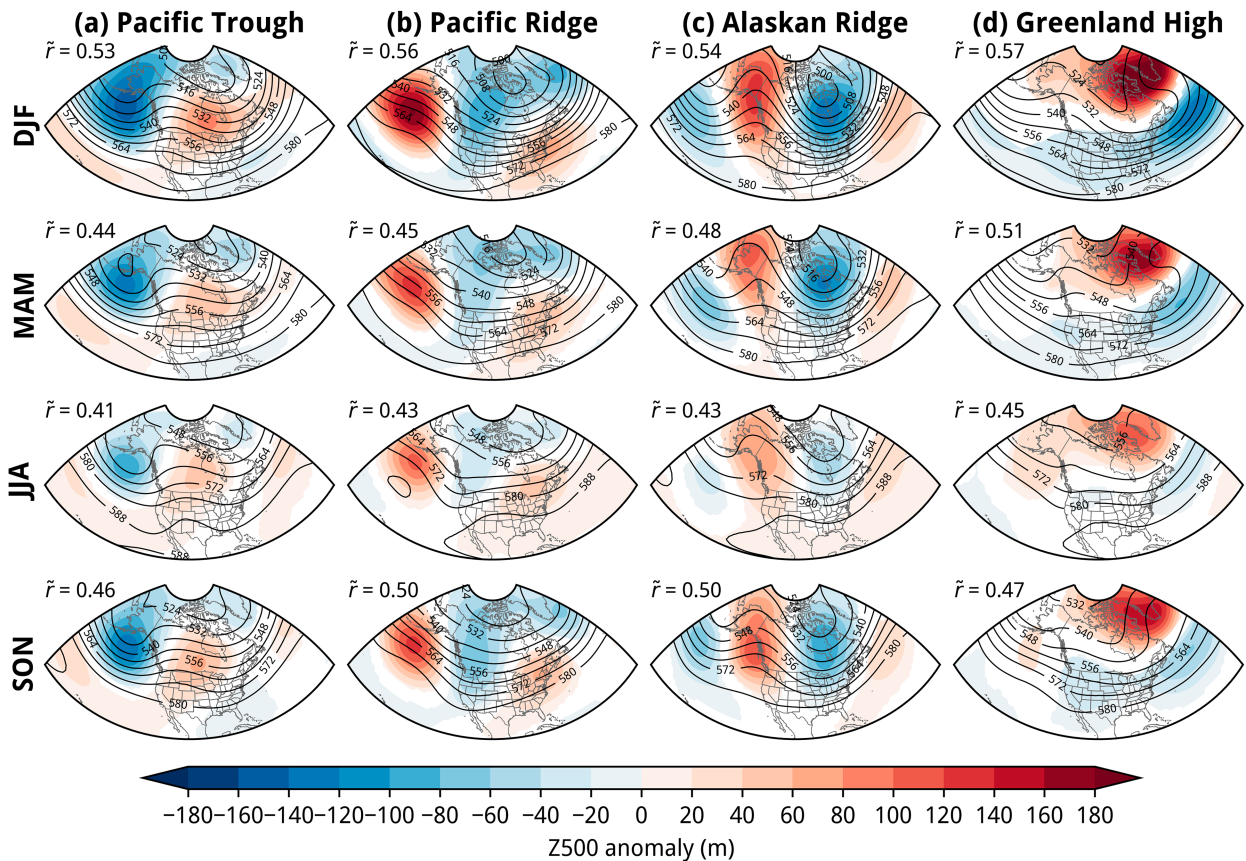
FIG. 10. (a)–(d) Seasonal variation (rows) in the average Z500 anomalies (shading; m) and mean Z500 (black contours; dam) associated with the four regimes. In each panel, the median area-weighted pattern correlation ($\tilde{r}$) of all days assigned to each regime per season with the seasonal mean is shown in the top left. Data are masked where not significantly different from zero at the 95% confidence level according to a block bootstrap resampling test.

weighted pattern correlations exceed 0.90, except for PT during MAM ($r = 0.86$). The median pattern correlations for all days assigned to each seasonally dependent regime are indistinguishable from those shown in Fig. 10: they also exhibit the same small seasonal cycle with a summertime minimum, confirming that this is likely an effect of less structured summertime variability. Therefore, since no other patterns appear when constructing separate regimes for each season, we see no benefit in a seasonally dependent classification. Indeed, aside from simple continuity, the year-round method also benefits from a larger sample size, which may yield greater cluster stability (Michelangeli et al. 1995), and is not influenced by the rapid changes in field variance during spring and autumn.

g. Links to meteorological conditions

We now link the circulation anomalies in each regime to relevant meteorological variables. Figures 11 and 12, respectively, show the average anomalies of daily 2-m air temperature and precipitation for all days assigned to each regime in each season. In general, since the circulation anomalies do not markedly change season-to-season, neither do the accompanying temperature and precipitation anomaly patterns.

The PT regime is associated with the most widespread above-average temperatures (Fig. 11a), centered in western Canada. Only western Alaska typically experiences temperatures substantially below normal during this regime. Precipitation is well above normal along the west coast, particularly from Oregon to southern Alaska (Fig. 12a), but generally below normal across the central continent under the anomalous ridge. The PT regime is the only regime associated with widely above-normal west coast precipitation, which has been previously linked to above-normal atmospheric river frequency in winter (Amini and Straus 2019).

The PR regime is characterized by a northwest–southeast dipole in temperature anomalies (Fig. 11b), with colder than normal conditions along the West Coast, western Canada, and Alaska, and warmer than normal conditions across the eastern United States and Canada. Indeed, in the east/southeast, the PR regime is on average the warmest, while it is on average the coldest for the west/northwest. Precipitation is slightly above normal in the interior of the continent, and generally near or below normal along the west coast (Fig. 12b).

The AKR regime is on average the coldest for the eastern half of the continent (Fig. 11c), while the west coast and Alaska (where the AKR regime is the warmest) experience
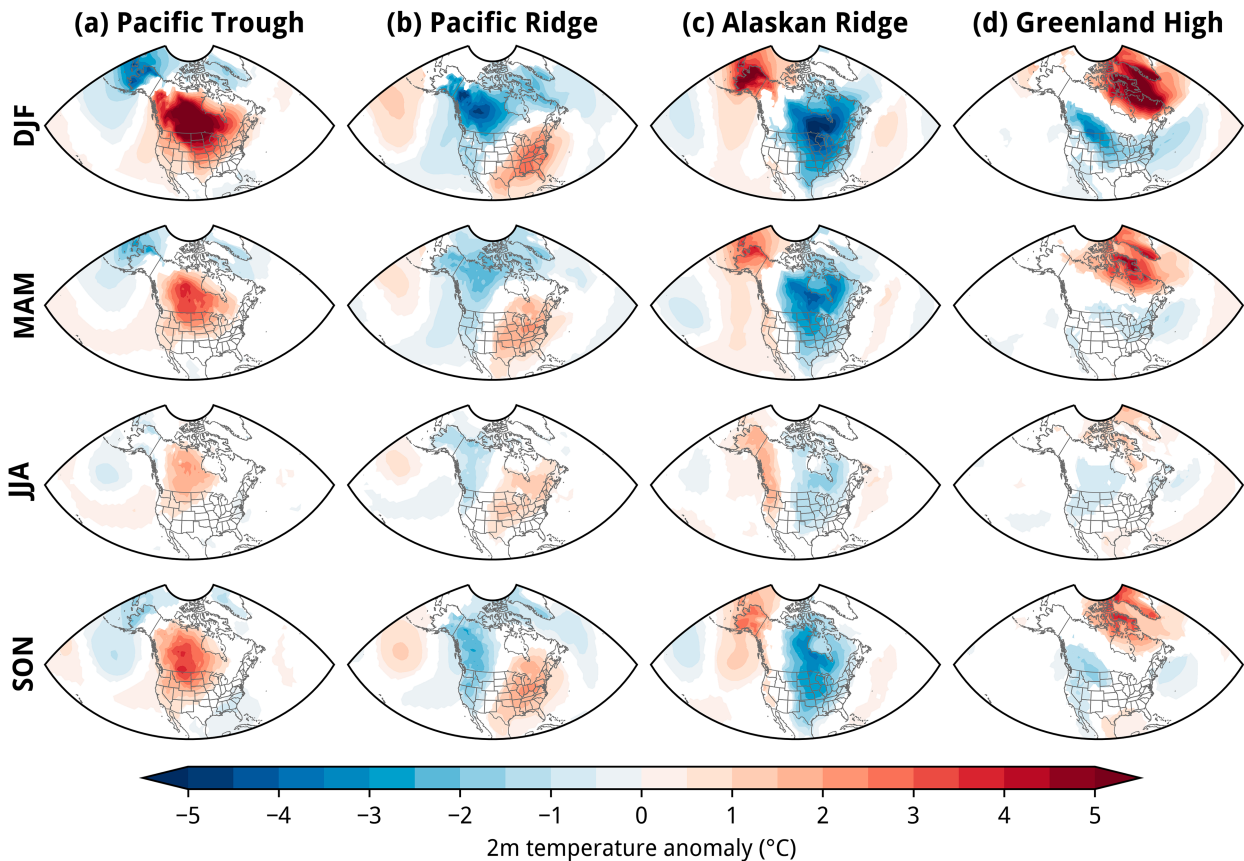
FIG. 11. (a)–(d) Seasonal variation (rows) in the average 2-m temperature anomalies associated with the four regimes. Data are masked where not significantly different from zero at the 95% confidence level according to a block bootstrap resampling test.

above normal temperatures. The relationship between the AKR regime and extreme cold in winter has been previously reported (S. H. Lee et al. 2019; Millin et al. 2022; Messori et al. 2022). During summer, above-average temperatures during the AKR regime are more extensive in the Pacific Northwest compared to other seasons. The AKR regime is the driest regime for the west coast and many interior parts of the continent, and nominally the wettest for the east coast (Fig. 12c).

During the GH regime, average temperature anomalies (Fig. 11d) are substantially more pronounced during winter when anomalously cold conditions dominate the United States and southern Canada; these are comparatively minimal during other seasons, especially summer. Aside from over the Atlantic off the U.S. East Coast, the GH regime is on average the coldest regime for only a small region of northwestern Mexico extending up the Continental Divide to southern Wyoming, while it is the warmest regime for regions surrounding the Labrador Sea. Large precipitation anomalies (Fig. 12d) are mostly confined to the coast of British Columbia (BC), which is significantly drier than average during the GH regime. During winter and early spring, the GH regime is more likely when the stratospheric polar vortex is weak (S. H. Lee et al. 2019), and so the dry conditions along the BC coast are consistent with the locally reduced atmospheric river frequency during weak vortex conditions (Lee et al. 2022b).

h. Interannual-to-decadal variability

Finally, we assess variability and trends in the frequency of the regimes since 1979. Changes to regime frequency, rather than their structure, are an expected response of the climate system to an external forcing (Palmer 1999). Here we report, but do not attribute, the observed trends.

The annual frequency of each regime is shown in Figs. 13a–e. The number of days assigned to the PT regime (Fig. 13a) has decreased since 1979 at a rate of -5.4 days decade^{-1} ($p = 0.09$), with an average of 28 days fewer PT regime days per year in the last 10 years compared with the first 10 years. The trend in the frequency of the PT regime is consistent with the residual circulation trend in the Z500 data (Fig. 1c), which resembles the inverse of the PT regime (cf. Fig. 3a). No other regime, nor the No Regime state, shows significant annual trends. Hence, the decreasing frequency of the PT regime is not associated with a concomitant increase of one other regime, but rather a general increase in the combined frequency of the four other classifications. When taken together, this is broadly consistent with the "fewer troughs, not more ridges" conclusion of Zhang et al. (2022) using five weather types over a smaller, CONUS-focused domain.

The 10-yr moving averages in Figs. 13c and 13d also suggest that the AKR and GH regimes exhibit pronounced multiannual
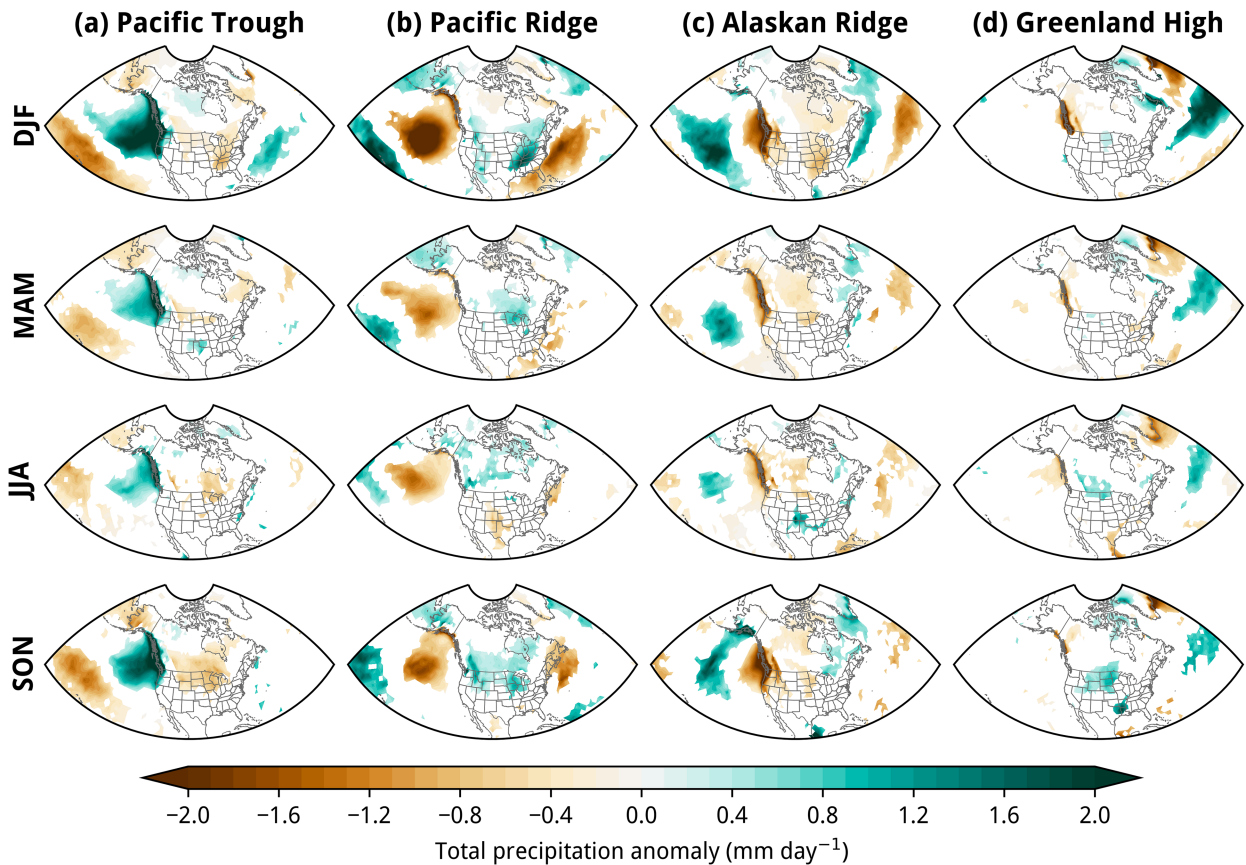
FIG. 12. (a)–(d) Seasonal variation (rows) in the average daily total precipitation anomalies associated with the four regimes. Data are masked where not significantly different from zero at the 95% confidence level according to a block bootstrap resampling test.

variability in approximate antiphase: GH frequency was lower in the late 1980s–early 1990s and maximized in the late 2000s–early 2010s, with the opposite variability for the AKR regime. This is broadly consistent with observed variability in the NAO (and the closely related Arctic Oscillation) from a predominantly positive phase in the early 1990s to a more negative phase by the late 2000s (Pinto and Raible 2012).

To assess whether the trends in annual frequency arise from a specific season or are disguising competing trends between seasons, we show the seasonal frequency trends in Fig. 13f. We find that the large annual-scale decline in the frequency of the PT regime has occurred due to a general decline in all seasons, most robustly in spring (-2.0 days decade^{-1}; $p = 0.09$). There has been a significant increase in AKR regime frequency during spring (2.1 days decade^{-1}; $p = 0.05$), but this is effectively offset by an equivalent decrease in summer (-2.0 days decade^{-1}; $p = 0.03$). The largest trend is an increase in summertime GH frequency of 3.9 days decade^{-1} ($p = 0.01$), equating to 21% of the 1979–2022 average JJA frequency per decade. Such a trend is consistent with the observed weakening of the midlatitude summertime westerly flow (Coumou et al. 2015), but the apparent multidecadal variability in GH frequency implies a large role for internal variability as is typical of the NAO (e.g., Deser et al. 2017).

5. Summary and conclusions

In this study, we have constructed a new set of four year-round weather regimes for North America using k-means clustering. A crucial step in their construction was the normalization of the Z500 anomalies by the seasonal cycle in the domain-average variance (Fig. 1), in order to give equal weight to summer and winter variability in the clustering procedure. The choice of k clusters was motivated by agreement between four separate objective methods, which all supported four clusters as the best choice (Fig. 2). Because naive k-means clustering assigns every day to a regime—and thus even days with minimal circulation anomalies—we then applied an objective No Regime criterion by defining a new centroid to represent climatology, which accounts for 14% of days overall.

The Z500 anomaly patterns obtained for our four new regimes closely resemble regimes previously defined for the winter and summer seasons separately, indicating that the regimes present over North America do not differ markedly between the warm and cold seasons. Such a conclusion has been previously suggested (Nabizadeh et al. 2022) but has not been explicitly demonstrated from a year-round perspective. In addition, while our new regimes were computed in the space spanned by the leading 12 PCs (81% explained variance), only the leading three (39% explained variance) were found to play an important role (Fig. 5). Indeed, the four weather
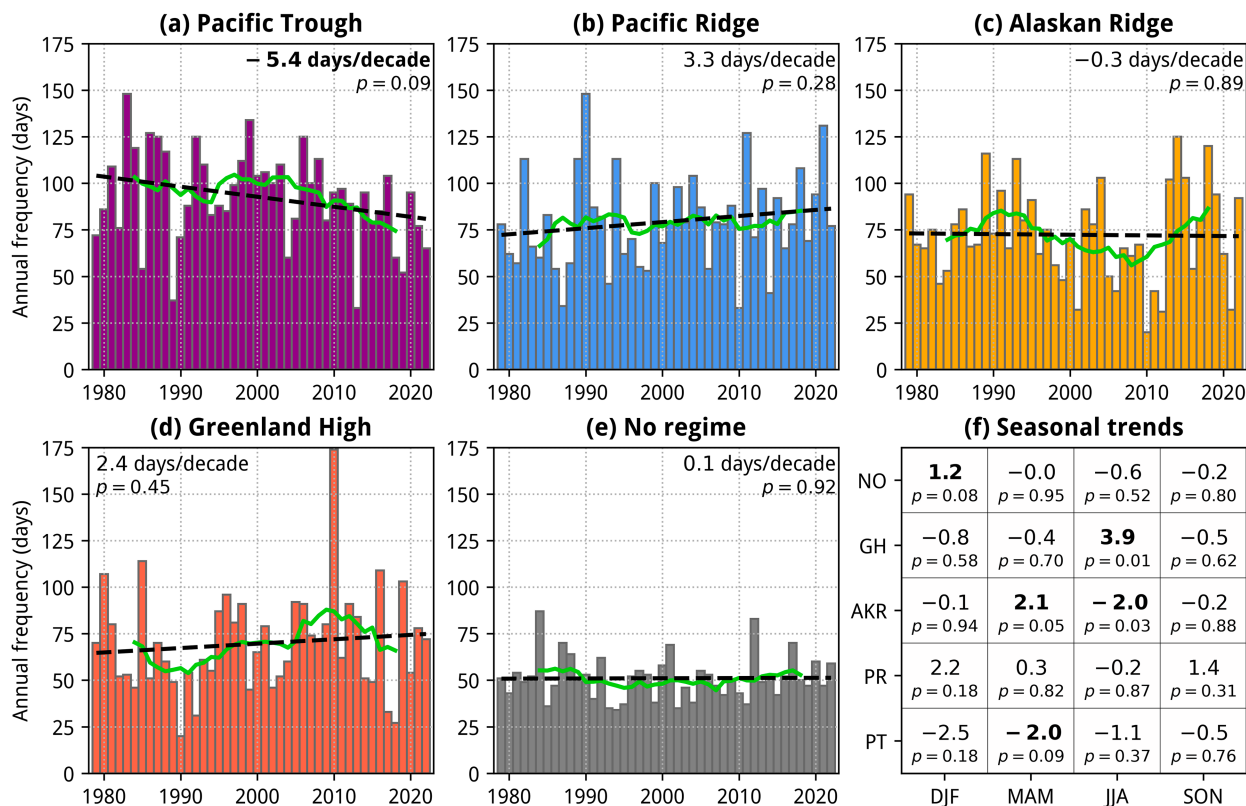
FIG. 13. (a)–(e) Time series of the number of days per year (bars) assigned to each regime. Green lines show 10-yr centered running means, and the black dashed lines denote the linear trends. The slope of the linear regression and the associated p value (obtained by bootstrapping 10 000 times with replacement) are also shown. (f) Linear trends (days decade^{-1}) in the frequency of each regime in each season. Trends are shown in bold where $p < 0.10$.

regimes themselves explain a similar fraction of the total variance (43%; obtained by projecting the low-pass-filtered normalized Z500 anomalies onto an orthogonal basis set created with the Gram–Schmidt method). Hence, we caution that one should not infer the amount of variance explained by the regimes simply from the variance explained by the PCs used as the basis set for the clustering. Rather, the dominance of only three PCs indicates that regime behavior is likely to be adequately described by this much-truncated set, while higher-order PCs simply represent weather noise.

We found that the regimes were persistent, with a median residence time of 6–7 days (Fig. 6), roughly three times more persistent than No Regime. Such persistence was obtained without imposing a subjective persistence criterion, indicating that naturally persistent states are detected by the classification. Instances of regimes persisting for more than two weeks have occurred in all seasons, and individual regimes lasting for more than four weeks have occurred in the record for all but the AKR regime. The association between long-lived regimes and windows of opportunity for extended-range prediction is a potential avenue for further study, with our year-round regimes providing a novel ability to do so in all seasons. Additionally, because our regimes extend directly into the North Atlantic, the potential exists for considering the link to downstream impacts on the NAE regimes and European

weather. For example, a recent study by Riboldi et al. (2023) linked two North American weather patterns that resemble the GH and AKR regimes with cold spells over North America and downstream European windstorms.

The linkage between long-lived regimes, extreme events and their predictability is also noteworthy, as subseasonal forecasts provide the requisite lead time to implement proactive mitigation measures (e.g., Vitart and Robertson 2018). Here we present two motivating examples. The longest-lasting PT regime (43 days from 14 January to 25 February 1998; see Fig. 4) occurred during an extreme El Niño winter (Wolter and Timlin 1998) and was associated with the warmest and wettest January–February on record for CONUS at the time (Ross et al. 1998). Given that the PT regime is more likely during El Niño (Fig. 8) and is the only regime associated with increased precipitation along the west coast of North America (Fig. 12), then potential predictability of such extremes may exist. More recently, the longest-lasting AKR regime to begin in June (during its climatological minimum; Fig. 9) was 10 consecutive days from 17 to 26 June 2021 inclusive, immediately prior to the peak of the extreme Pacific Northwest heatwave (26–29 June, during which the PT regime was present). The warm and dry average conditions during the AKR regime (Figs. 11c and 12c) are consistent with generating the precursor soil moisture conditions which played a role in the extreme nature of the heatwave (Schumacher et al. 2022).

The association between the PT regime, El Niño and enhanced precipitation in western North America is notable given its decreasing frequency (Fig. 13), particularly since 2010 (which has coincided with an increase in the typically dry AKR regime). In a study of wintertime Pacific regimes in CMIP6 models, Fabiano et al. (2021) found an increase in PT frequency under future climate scenarios, potentially related to an increased frequency of El Niño. While this projected trend is in contrast to the observed trend, the models assessed by Fabiano et al. (2021) did show a decreased PT frequency in recent decades under historical forcing (their Fig. S10). This is despite the discrepancy between trends in the Walker circulation in models (strengthening) and observations (weakening) in recent decades (Wills et al. 2022). Given the additional large increase in summertime GH frequency (Fig. 13f), it would therefore be useful to extend the analysis of Fabiano et al. (2021) to the year-round definition, and to better understand the relative contributions of internal versus forced variability in the observed trends.

Regardless of whether these regimes represent true physical modes of the climate system, they remain a useful statistical tool for the characterization of large-scale, recurrent low-frequency flow anomalies. Condensing the vast and ongoing growth in subseasonal forecast data—such as the daily 101-member forecasts from the cycle 48r1 upgrade to the ECMWF prediction system (Vitart et al. 2022)—into a comprehensible format poses a significant challenge. Regimes present perhaps the simplest objective framework through which operational forecasters and research scientists can easily understand the distribution of all ensemble members, their run-to-run differences, and assess flow-dependent predictability (Matsueda and Palmer 2018; Nabizadeh et al. 2022). Furthermore, much like the success of the "atmospheric river" terminology in multidisciplinary science and public communication (Ralph et al. 2020), the comparable simplicity of the regimes framework may prove similarly useful in communicating subseasonal forecasts and large-scale climate variability with decision-makers and the public alike.

In conclusion, we contend that the novel regimes classification defined herein can be applied, in a straightforward manner, to a variety of weather and climate problems. In particular, hazardous phenomena such as severe convective weather that occur year-round—especially during the spring and autumn, when regimes have as yet been ill-defined—seem particularly well suited. We plan to address this in a subsequent study.

Data availability statement. ERA5 reanalysis data are freely available from the Copernicus Climate Data Store (https://cds.climate.copernicus.eu/). The calculated regimes data are freely available on Zenodo at https://doi.org/10.5281/zenodo.8165165.

REFERENCES

Amini, S., and D. M. Straus, 2019: Control of storminess over the Pacific and North America by circulation regimes: The role of large-scale dynamics in weather extremes. *Climate Dyn.*, **52**, 4749–4770, https://doi.org/10.1007/s00382-018-4409-7.

Bao, M., and J. M. Wallace, 2015: Cluster analysis of Northern Hemisphere wintertime 500-hPa flow regimes during 1920–2014. *J. Atmos. Sci.*, **72**, 3597–3608, https://doi.org/10.1175/JAS-D-15-0001.1.

Black, R. X., B. A. McDaniel, and W. A. Robinson, 2006: Stratosphere–troposphere coupling during spring onset. *J. Climate*, **19**, 4891–4901, https://doi.org/10.1175/JCLI3907.1.

Büeler, D., L. Ferranti, L. Magnusson, J. F. Quinting, and C. M. Grams, 2021: Year-round sub-seasonal forecast skill for Atlantic–European weather regimes. *Quart. J. Roy. Meteor. Soc.*, **147**, 4283–4309, https://doi.org/10.1002/qj.4178.

Butler, A. H., and D. I. V. Domeisen, 2021: The wave geometry of final stratospheric warming events. *Wea. Climate Dyn.*, **2**, 453–474, https://doi.org/10.5194/wcd-2-453-2021.

Cassou, C., 2008: Intraseasonal interaction between the Madden–Julian Oscillation and the North Atlantic Oscillation. *Nature*, **455**, 523–527, https://doi.org/10.1038/nature07286.

——, L. Terray, J. W. Hurrell, and C. Deser, 2004: North Atlantic winter climate regimes: Spatial asymmetry, stationarity with time, and oceanic forcing. *J. Climate*, **17**, 1055–1068, https://doi.org/10.1175/1520-0442(2004)017<1055:NAWCRS>2.0.CO;2.

Charney, J. G., and J. G. DeVore, 1979: Multiple flow equilibria in the atmosphere and blocking. *J. Atmos. Sci.*, **36**, 1205–1216, https://doi.org/10.1175/1520-0469(1979)036<1205:MFEITA>2.0.CO;2.

Cheng, X., and J. M. Wallace, 1993: Cluster analysis of the Northern Hemisphere wintertime 500-hPa height field: Spatial patterns. *J. Atmos. Sci.*, **50**, 2674–2696, https://doi.org/10.1175/1520-0469(1993)050<2674:CAOTNH>2.0.CO;2.

Christiansen, B., 2007: Atmospheric circulation regimes: Can cluster analysis provide the number? *J. Climate*, **20**, 2229–2250, https://doi.org/10.1175/JCLI4107.1.

Coe, D., M. Barlow, L. Agel, F. Colby, C. Skinner, and J.-H. Qian, 2021: Clustering analysis of autumn weather regimes in the Northeast United States. *J. Climate*, **34**, 7587–7605, https://doi.org/10.1175/JCLI-D-20-0243.1.

Coumou, D., J. Lehmann, and J. Beckmann, 2015: The weakening summer circulation in the Northern Hemisphere mid-latitudes. *Science*, **348**, 324–327, https://doi.org/10.1126/science.1261768.

Davies, D. L., and D. W. Bouldin, 1979: A cluster separation measure. *IEEE Trans. Pattern Anal. Mach. Intell.*, **PAMI-1**, 224–227, https://doi.org/10.1109/TPAMI.1979.4766909.

Deser, C., J. W. Hurrell, and A. S. Phillips, 2017: The role of the North Atlantic Oscillation in European climate projections. *Climate Dyn.*, **49**, 3141–3157, https://doi.org/10.1007/s00382-016-3502-z.

Dorrington, J., K. Strommen, F. Fabiano, and F. Molteni, 2022: CMIP6 models trend toward less persistent European blocking regimes in a warming climate. *Geophys. Res. Lett.*, **49**, e2022GL100811, https://doi.org/10.1029/2022GL100811.

Fabiano, F., V. L. Meccia, P. Davini, P. Ghinassi, and S. Corti, 2021: A regime view of future atmospheric circulation

changes in northern mid-latitudes. *Wea. Climate Dyn.*, **2**, 163–180, https://doi.org/10.5194/wcd-2-163-2021.

Fereday, D. R., 2017: How persistent are North Atlantic–European sector weather regimes? *J. Climate*, **30**, 2381–2394, https://doi.org/10.1175/JCLI-D-16-0328.1.

——, J. R. Knight, A. A. Scaife, C. K. Folland, and A. Philipp, 2008: Cluster analysis of North Atlantic–European circulation types and links with tropical Pacific sea surface temperatures. *J. Climate*, **21**, 3687–3703, https://doi.org/10.1175/2007JCLI1875.1.

Francis, J. A., N. Skific, and S. J. Vavrus, 2018: North American weather regimes are becoming more persistent: Is Arctic amplification a factor? *Geophys. Res. Lett.*, **45**, 11 414–11 422, https://doi.org/10.1029/2018GL080252.

Grams, C. M., R. Beerli, S. Pfenninger, I. Staffell, and H. Wernli, 2017: Balancing Europe's wind-power output through spatial deployment informed by weather regimes. *Nat. Climate Change*, **7**, 557–562, https://doi.org/10.1038/nclimate3338.

——, L. Ferranti, and L. Magnusson, 2020: How to make use of weather regimes in extended-range predictions for Europe. *ECMWF Newsletter*, No. 165, ECMWF, Reading, United Kingdom, 14–19, www.ecmwf.int/en/newsletter/165/meteorology/how-make-use-weather-regimes-extended-range-predictions-europe.

Hannachi, A., D. M. Straus, C. L. E. Franzke, S. Corti, and T. Woollings, 2017: Low-frequency nonlinearity and regime behavior in the Northern Hemisphere extratropical atmosphere. *Rev. Geophys.*, **55**, 199–234, https://doi.org/10.1002/2015RG000509.

Hersbach, H., and Coauthors, 2020: The ERA5 global reanalysis. *Quart. J. Roy. Meteor. Soc.*, **146**, 1999–2049, https://doi.org/10.1002/qj.3803.

Hochman, A., G. Messori, J. F. Quinting, J. G. Pinto, and C. M. Grams, 2021: Do Atlantic-European weather regimes physically exist? *Geophys. Res. Lett.*, **48**, e2021GL095574, https://doi.org/10.1029/2021GL095574.

Hurrell, J. W., and C. Deser, 2010: North Atlantic climate variability: The role of the North Atlantic Oscillation. *J. Mar. Syst.*, **79**, 231–244, https://doi.org/10.1016/j.jmarsys.2009.11.002.

Huth, R., C. Beck, A. Philipp, M. Demuzere, Z. Ustrnul, M. Cahynová, J. Kyselý, and O. E. Tveito, 2008: Classifications of atmospheric circulation patterns: Recent advances and applications. *Ann. N. Y. Acad. Sci.*, **1146**, 105–152, https://doi.org/10.1196/annals.1446.019.

Kimoto, M., and M. Ghil, 1993: Multiple flow regimes in the Northern Hemisphere winter. Part I: Methodology and hemispheric regimes. *J. Atmos. Sci.*, **50**, 2625–2644, https://doi.org/10.1175/1520-0469(1993)050<2625:MFRITN>2.0.CO;2.

Lamb, H. H., 1950: Types and spells of weather around the year in the British Isles: Annual trends, seasonal structure of the year, singularities. *Quart. J. Roy. Meteor. Soc.*, **76**, 393–429, https://doi.org/10.1002/qj.49707633005.

Lee, R. W., S. J. Woolnough, A. J. Charlton-Perez, and F. Vitart, 2019: ENSO modulation of MJO teleconnections to the North Atlantic and Europe. *Geophys. Res. Lett.*, **46**, 13 535–13 545, https://doi.org/10.1029/2019GL084683.

Lee, S. H., J. C. Furtado, and A. J. Charlton-Perez, 2019: Wintertime North American weather regimes and the Arctic stratospheric polar vortex. *Geophys. Res. Lett.*, **46**, 14 892–14 900, https://doi.org/10.1029/2019GL085592.

——, A. J. Charlton-Perez, S. J. Woolnough, and J. C. Furtado, 2022a: How do stratospheric perturbations influence North American weather regime predictions? *J. Climate*, **35**, 5915–5932, https://doi.org/10.1175/JCLI-D-21-0413.1.

——, L. M. Polvani, and B. Guan, 2022b: Modulation of atmospheric rivers by the Arctic stratospheric polar vortex. *Geophys. Res. Lett.*, **49**, e2022GL100381, https://doi.org/10.1029/2022GL100381.

Lembo, V., F. Fabiano, V. M. Galfi, R. G. Graversen, V. Lucarini, and G. Messori, 2022: Meridional-energy-transport extremes and the general circulation of Northern Hemisphere mid-latitudes: Dominant weather regimes and preferred zonal wavenumbers. *Wea. Climate Dyn.*, **3**, 1037–1062, https://doi.org/10.5194/wcd-3-1037-2022.

Levick, R. B. M., 1949: Fifty years of English weather. *Weather*, **4**, 206–211, https://doi.org/10.1002/j.1477-8696.1949.tb05487.x.

——, 1950: Fifty years of British weather. *Weather*, **5**, 245–247, https://doi.org/10.1002/j.1477-8696.1950.tb01207.x.

Mariotti, A., and Coauthors, 2020: Windows of opportunity for skillful forecasts subseasonal to seasonal and beyond. *Bull. Amer. Meteor. Soc.*, **101**, E608–E625, https://doi.org/10.1175/BAMS-D-18-0326.1.

Matsueda, M., and T. N. Palmer, 2018: Estimates of flow-dependent predictability of wintertime Euro-Atlantic weather regimes in medium-range forecasts. *Quart. J. Roy. Meteor. Soc.*, **144**, 1012–1027, https://doi.org/10.1002/qj.3265.

Messori, G., M. Kretschmer, S. H. Lee, and V. Wendt, 2022: Stratospheric downward wave reflection events modulate North American weather regimes and cold spells. *Wea. Climate Dyn.*, **3**, 1215–1236, https://doi.org/10.5194/wcd-3-1215-2022.

Michelangeli, P.-A., R. Vautard, and B. Legras, 1995: Weather regimes: Recurrence and quasi stationarity. *J. Atmos. Sci.*, **52**, 1237–1256, https://doi.org/10.1175/1520-0469(1995)052<1237:WRRAQS>2.0.CO;2.

Miller, D. E., Z. Wang, R. J. Trapp, and D. S. Harnos, 2020: Hybrid prediction of weekly tornado activity out to Week 3: Utilizing weather regimes. *Geophys. Res. Lett.*, **47**, e2020GL087253, https://doi.org/10.1029/2020GL087253.

Millin, O. T., J. C. Furtado, and J. B. Basara, 2022: Characteristics, evolution, and formation of cold air outbreaks in the Great Plains of the United States. *J. Climate*, **35**, 4585–4602, https://doi.org/10.1175/JCLI-D-21-0772.1.

Molina, M. J., J. H. Richter, A. A. Glanville, K. Dagon, J. Berner, A. Hu, and G. A. Meehl, 2023: Subseasonal representation and predictability of North American weather regimes using cluster analysis. *Artif. Intell. Earth Syst.*, **2**, e220051, https://doi.org/10.1175/AIES-D-22-0051.1.

Molteni, F., L. Ferranti, T. Palmer, and P. Viterbo, 1993: A dynamical interpretation of the global response to equatorial Pacific SST anomalies. *J. Climate*, **6**, 777–795, https://doi.org/10.1175/1520-0442(1993)006<0777:ADIOTG>2.0.CO;2.

Nabizadeh, E., S. W. Lubis, and P. Hassanzadeh, 2022: The summertime Pacific-North American weather regimes and their predictability. *Geophys. Res. Lett.*, **49**, e2022GL099401, https://doi.org/10.1029/2022GL099401.

Neal, R., D. Fereday, R. Crocker, and R. E. Comer, 2016: A flexible approach to defining weather patterns and their application in weather forecasting over Europe. *Meteor. Appl.*, **23**, 389–400, https://doi.org/10.1002/met.1563.

Palmer, T. N., 1999: A nonlinear dynamical perspective on climate prediction. *J. Climate*, **12**, 575–591, https://doi.org/10.1175/1520-0442(1999)012<0575:ANDPOC>2.0.CO;2.

Pasquier, J. T., S. Pfahl, and C. M. Grams, 2019: Modulation of atmospheric river occurrence and associated precipitation

extremes in the North Atlantic region by European weather regimes. *Geophys. Res. Lett.*, **46**, 1014–1023, https://doi.org/10.1029/2018GL081194.

Pedregosa, F., and Coauthors, 2011: Scikit-learn: Machine learning in Python. *J. Mach. Learn. Res.*, **12**, 2825–2830.

Pinto, J. G., and C. C. Raible, 2012: Past and recent changes in the North Atlantic Oscillation. *Wiley Interdiscip. Rev.: Climate Change*, **3**, 79–90, https://doi.org/10.1002/wcc.150.

Ralph, F. M., M. D. Dettinger, J. J. Rutz, and D. E. Waliser, 2020: *Atmospheric Rivers*. 1st ed. Springer, 252 pp.

Reusch, D. B., R. B. Alley, and B. C. Hewitson, 2007: North Atlantic climate variability from a self-organizing map perspective. *J. Geophys. Res.*, **112**, D02104, https://doi.org/10.1029/2006JD007460.

Rex, D. F., 1951: The effect of Atlantic blocking action upon European climate. *Tellus*, **3**, 100–112, https://doi.org/10.3402/tellusa.v3i2.8617.

Riboldi, J., R. Leeding, A. Segalini, and G. Messori, 2023: Multiple large-scale dynamical pathways for Pan–Atlantic compound cold and windy extremes. *Geophys. Res. Lett.*, **50**, e2022GL102528, https://doi.org/10.1029/2022GL102528.

Robertson, A. W., N. Vigaud, J. Yuan, and M. K. Tippett, 2020: Toward identifying subseasonal forecasts of opportunity using North American weather regimes. *Mon. Wea. Rev.*, **148**, 1861–1875, https://doi.org/10.1175/MWR-D-19-0285.1.

Ross, T., N. Lott, S. McCown, and D. Quinn, 1998: The El Nino winter of '97-'98. NCDC Tech. Rep. 98-02, 28 pp., https://repository.library.noaa.gov/view/noaa/13823.

Rousi, E., F. Selten, S. Rahmstorf, and D. Coumou, 2021: Changes in North Atlantic atmospheric circulation in a warmer climate favor winter flooding and summer drought over Europe. *J. Climate*, **34**, 2277–2295, https://doi.org/10.1175/JCLI-D-20-0311.1.

Schumacher, D. L., M. Hauser, and S. I. Seneviratne, 2022: Drivers and mechanisms of the 2021 Pacific Northwest heatwave. *Earth's Future*, **10**, e2022EF002967, https://doi.org/10.1029/2022EF002967.

Sheridan, S. C., 2002: The redevelopment of a weather-type classification scheme for North America. *Int. J. Climatol.*, **22**, 51–68, https://doi.org/10.1002/joc.709.

Son, S.-W., H. Kim, K. Song, S.-W. Kim, P. Martineau, Y.-K. Hyun, and Y. Kim, 2020: Extratropical prediction skill of the subseasonal-to-seasonal (S2S) prediction models. *J. Geophys. Res. Atmos.*, **125**, e2019JD031273, https://doi.org/10.1029/2019JD031273.

Spensberger, C., and Coauthors, 2020: Dynamics of concurrent and sequential Central European and Scandinavian heatwaves. *Quart. J. Roy. Meteor. Soc.*, **146**, 2998–3013, https://doi.org/10.1002/qj.3822.

Stephenson, D. B., A. Hannachi, and A. O'Neill, 2004: On the existence of multiple climate regimes. *Quart. J. Roy. Meteor. Soc.*, **130**, 583–605, https://doi.org/10.1256/qj.02.146.

Straus, D. M., S. Corti, and F. Molteni, 2007: Circulation regimes: Chaotic variability versus SST-forced predictability. *J. Climate*, **20**, 2251–2272, https://doi.org/10.1175/JCLI4070.1.

Tippett, M. K., and A. G. Barnston, 2008: Skill of multimodel ENSO probability forecasts. *Mon. Wea. Rev.*, **136**, 3933–3946, https://doi.org/10.1175/2008MWR2431.1.

Vautard, R., 1990: Multiple weather regimes over the North Atlantic: Analysis of precursors and successors. *Mon. Wea. Rev.*, **118**, 2056–2081, https://doi.org/10.1175/1520-0493(1990)118<2056:MWROTN>2.0.CO;2.

Vigaud, N., A. W. Robertson, and M. K. Tippett, 2018: Predictability of recurrent weather regimes over North America during winter from submonthly reforecasts. *Mon. Wea. Rev.*, **146**, 2559–2577, https://doi.org/10.1175/MWR-D-18-0058.1.

Vitart, F., and A. W. Robertson, 2018: The sub-seasonal to seasonal prediction project (S2S) and the prediction of extreme events. *npj Climate Atmos. Sci.*, **1**, 3, https://doi.org/10.1038/s41612-018-0013-0.

——, M. A. Balmaseda, L. Ferranti, and M. Fuentes, 2022: The next extended-range configuration for IFS Cycle 48r1. *ECMWF Newsletter*, No. 173, ECMWF, Reading, United Kingdom, 21–26, https://www.ecmwf.int/en/newsletter/173/earth-system-science/next-extended-range-configuration-ifs-cycle-48r1.

Wallace, J. M., Y. Zhang, and K.-H. Lau, 1993: Structure and seasonality of interannual and interdecadal variability of the geopotential height and temperature fields in the Northern Hemisphere troposphere. *J. Climate*, **6**, 2063–2082, https://doi.org/10.1175/1520-0442(1993)006<2063:SASOIA>2.0.CO;2.

White, C. J., and Coauthors, 2021: Advances in the application and utility of subseasonal-to-seasonal predictions. *Bull. Amer. Meteor. Soc.*, **103**, E1448–E1472, https://doi.org/10.1175/BAMS-D-20-0224.1.

Wills, R. C. J., Y. Dong, C. Proistosecu, K. C. Armour, and D. S. Battisti, 2022: Systematic climate model biases in the large-scale patterns of recent sea-surface temperature and sea-level pressure change. *Geophys. Res. Lett.*, **49**, e2022GL100011, https://doi.org/10.1029/2022GL100011.

Wolter, K., and M. S. Timlin, 1998: Measuring the strength of ENSO events: How does 1997/98 rank? *Weather*, **53**, 315–324, https://doi.org/10.1002/j.1477-8696.1998.tb06408.x.

Zhang, W., and G. Villarini, 2019: On the weather types that shape the precipitation patterns across the U.S. Midwest. *Climate Dyn.*, **53**, 4217–4232, https://doi.org/10.1007/s00382-019-04783-4.

——, V. Hari, S. S.-Y. Wang, M. D. LaPlante, G. Garfin, G. Affram, and R. Kumar, 2022: Fewer troughs, not more ridges, have led to a drying trend in the western United States. *Geophys. Res. Lett.*, **49**, e2021GL097089, https://doi.org/10.1029/2021GL097089.